Field-Induced Phase Transition of the Spin Liquid State in Triangular Antiferromagnet $YbMgGaO_4$

Authors: William M. Steinhardt[1], Zhenzhong Shi[1], Anjana Samarakoon[2,3], Sachith Dissanayake[1,3], David Graf[4], Yaohua Liu[3], Wei Zhu[5,6], Casey Marjerrison[1], Cristian D. Batista[2,7], Sara Haravifard[1,8*]

Affiliations:

[1] Department of Physics, Duke University, Durham, North Carolina 27708, USA.

[2] Shull-Wollan Center, Oak Ridge National Laboratory, Oak Ridge, Tennessee 37831, USA.

[3] Neutron Scattering Division, Oak Ridge National Laboratory, Oak Ridge, Tennessee 37831, USA.

[4] National High Magnetic Field Laboratory and Department of Physics, Florida State University, Tallahassee, Florida 32310, USA.

[5] Theoretical Division, T-4 & CNLS, Los Alamos National Laboratory, Los Alamos, New Mexico 87545, USA.

[6] Westlake Institute of Advanced Study, Hangzhou 310024, China.

[7] Department of Physics, University of Tennessee, Knoxville, Tennessee 37996, USA.

[8] Department of Mechanical Engineering and Materials Science, Duke University, Durham, North Carolina 27708, USA.

* Correspondence to: haravifard@phy.duke.edu

One Sentence Summary: Spin liquid state in a triangular antiferromagnet.

Abstract:

The triangular antiferromagnet $YbMgGaO_4$ has emerged as a candidate for hosting quantum spin liquid state, an exotic state of matter featuring a high degree of entanglement and often characterized as without magnetic ordering in the zero-temperature limit. However, the nature of the ground state in this system has been the subject of ardent debates, as recent work has shown that chemical disorder may contribute to quantum spin liquid-like features. Here we report a field-induced phase transition observed via diffuse neutron scattering and magnetic susceptibility

measurements. Comparisons to Monte Carlo simulations, using semi-classical spins and disorder, and Density Matrix Renormalization Group for the zero-temperature limit, reveal crucial information about the ground state and the roles that thermal fluctuations and chemical disorder play in the observed behavior.

Main text:

In the past few years the frustrated triangular antiferromagnet $YbMgGaO_4$ (Fig. S1) has been scrutinized as a possible host to the quantum spin liquid (QSL) state. While QSLs appear in many forms, a positive definition of QSLs is nearly as elusive as real-world examples (*1*). QSLs are usually identified by the absence of long-range order in the zero-temperature limit, and an exceptionally high degree of long-range entanglement (2). Thus, proving the existence of the QSL state is an exceptional experimental challenge, and to this date only few promising candidates are known (*2*). To that end, identifying probes to effectively examine the ground state of the QSL candidates is of utmost importance. Here we demonstrate that magnetic field can be utilized as an effective probe to shed light on the nature of ground states in QSL candidates. Furthermore, we discover the critical role of thermal fluctuations in this highly frustrated system, which are found to work alongside quenched disorder to create the observed spin liquid features.

Strong spin-orbit coupling and an odd number of electrons per unit cell have been identified as features conducive to exotic ground states (*2, 3*), bolstering $YbMgGaO_4$'s QSL candidacy. Consequently, a multitude of theoretical studies (*3-12*) and experimental techniques have sought to probe the phase diagram and elucidate the nature of the ground state (*13-22*). Recently, the effects of quenched disorder due to site-mixing between non-magnetic Mg^{2+} and Ga^{3+} have come under scrutiny (*5, 10, 16, 19*, *20*). Inelastic neutron scattering measurements have suggested that crystalline electric field (CEF) levels are broadened by a distribution of ytterbium-oxygen bond distances due to the Mg^{2+}/Ga^{3+} site mixing, leading to a distribution of effective spin-half g-factors and explaining the broadened low-energy magnetic excitations in the polarized state (*16*). Recent theoretical work suggests that, barring disorder in the charge environment from Mg^{2+}/Ga^{3+} site mixing, $YbMgGaO_4$ should have a collinear/stripe ground state (*5*). Furthermore, other calculations have suggested that the system should exhibit either a striped or 120° ordered state (*10*).

A missing piece of the puzzle of $YbMgGaO_4$'s low temperature behavior is the detailed study of its behavior in applied magnetic field. Anisotropy in magnetic interactions, field dependence, and the temperature dependence of magnetic features can provide invaluable information about the phase diagram of quantum magnetic materials. To that end, we measured static and dynamic properties of high-quality, single crystalline $YbMgGaO_4$ using the ultra-sensitive tunnel diode oscillation technique (TDO) (*24*), cantilever torque magnetometry, and diffuse neutron scattering. All three approaches provide evidence of a field-induced phase transition in $YbMgGaO_4$, providing critical insight into its magnetic ground state. We compare our results to complementary Monte Carlo (MC) and Density Matrix Renormalization Group (DMRG) calculations that further show the critical roles of disordered exchange interactions and g-factors, but also of thermal fluctuations, in producing the observed features.

The $YbMgGaO_4$ single crystal (Fig. S2) was grown using the optical floating zone technique. Rietveld refinement of powder X-ray diffraction measurements confirmed the pure phase (Fig. S3A), while Laue X-ray measurements (Fig. S3B) and neutron diffraction confirmed that the crystal was high-quality and single-grain. The magnetization and susceptibility results collected at temperatures down to $T = 1.8$ K (Fig. S4) were consistent with earlier reported results (*15, 17, 21*).

We performed ultra-high resolution magnetic susceptibility measurement on $YbMgGaO_4$ using TDO technique (Fig. S5A) up to fields exceeding saturation at temperatures down to 350 mK (Fig. 1). Comparison to cantilever torque magnetometry results (Fig. S5B) confirms the appearance of an anomaly near 2 T (Fig. 2C). The anomaly weakens with increasing temperature, vanishing near 4 K (Fig. 1A). The greater prominence of the feature in both techniques with applied field perpendicular (versus parallel) to the *c* axis (Fig. 1B) is consistent with easy-plane anisotropy found in earlier experiments (*15, 21, 25*). The anomaly is likely a remnant of the quantum mechanical 1/3 magnetization plateau, as will be discussed below.

To gain insight into the magnetic structure of the anomaly detected in the above measurements, and to explore its field dependence, we conducted diffuse neutron scattering with the *c* axis parallel to the field (Fig. 2A). We subtracted 20 K (background) signal from 130 mK data for integer fields from 0 to 5 T, isolating the magnetic contributions. To improve statistics and exploit 6-fold symmetry, we averaged intensity upon rotating in 60-degree steps about the *l*-axis (see Supplementary Materials for details, Fig. S6). After normalizing and accounting for a temperature scaling factor, integration over $-0.5 < l < 0.5$ in reciprocal space for zero field shows diffuse magnetic scattering at high-symmetry M points, indicative of short-range correlations and consistent with previous neutron measurements (*15, 17, 25*). With increasing field, the spectral weight shifts toward the K points – at $H = 1$ T the spectral weight is comparatively flat along the zone edge, while at $H = 2$ T the diffuse spectral weight is centered on the K points, likely corresponding to the feature in our magnetic susceptibility data (Fig. 1). When field is further increased, the scattering intensity at K points diminishes as the system approaches saturation. Integration of the spectral weight in a rectangular volume along the first Brillouin Zone (BZ) edge shows the shift in spectral weight from the M to K points and the reduction in intensity with increasing field (Fig. 2C).

Here we use a semi-classical approach to demonstrate that the lack of magnetic Bragg peaks and the broad continuum of magnetic excitations can be attributed to thermal fluctuations as well as chemical disorder. Main aspects of the observed phenomenology can be reproduced (Figs. 2B, 2D) with a classical spin model that reproduces the observed magnon dispersion above the saturation field (Fig. S7) and has long range magnetic ordering at $T = 0$ (Fig. S8). Moreover, we show that the reported disorder in the g-factor and in the exchange interactions (*16*) further contributes to the observed zero field broadening of the magnetic excitations (Fig. S7), raising doubts about the quantum versus classical nature of the observed spin liquid state in $YbMgGaO_4$.

We consider a classical limit of the spin Hamiltonian proposed in previous works (*22*):

$$H = \sum_{\langle ij\rangle}[J_{zz}S_i^zS_j^z + J_{\pm}(S_i^+S_j^- + S_i^-S_j^+) + J_{\pm\pm}(\gamma_{ij}S_i^+S_j^+ + \gamma_{ij}^*S_i^-S_j^-)$$

$$+\frac{i\,J_{z\pm}}{2}(\gamma_{ij}^*S_i^+S_j^z - \gamma_{ij}S_i^-S_j^z + \langle i \leftrightarrow j\rangle)] + \sum_{\langle\langle ij\rangle\rangle}[J_{2z}S_i^zS_j^z + J_{2\pm}(S_i^+S_j^- + S_i^-S_j^+)]$$

$$-\ \textstyle\sum_i\left[g_{\perp}(H^xS_i^x + H^yS_i^y) + g_{||}H^zS_i^z\right] \qquad (1)$$

where the phase factor $\gamma_{ij} = 1, e^{i2\pi/3}$ and $e^{-i2\pi/3}$, for each of the three principal directions of the triangular lattice. Thus, the interaction tensor of the classical Hamiltonian can be written as,

$$J_{ij} = \begin{bmatrix} 2J_{\pm} + 2J_{\pm\pm}cos(\gamma_{ij}) + 2J_{2\pm} & -2J_{\pm\pm}sin(\gamma_{ij}) & -J_{z\pm}sin(\gamma_{ij}) \\ -2J_{\pm\pm}sin(\gamma_{ij}) & 2J_{\pm} - 2J_{\pm\pm}cos(\gamma_{ij}) + 2J_{2\pm} & J_{z\pm}cos(\gamma_{ij}) \\ -J_{z\pm}sin(\gamma_{ij}) & J_{z\pm}cos(\gamma_{ij}) & J_{zz} + 2J_{2z} \end{bmatrix}$$

We consider a set of Hamiltonian parameters, $J_{\pm} = 0.66\,J_{zz}$, $J_{\pm\pm} = 0$, $J_{z\pm} = 0.13\,J_{zz}$, $J_{2z} = 0.1\,J_{zz}$, $J_{2\pm} = 0.066\,J_{zz}$ and $J_{zz} = 0.164$ meV, that reproduce the phenomenology. For the average g-factors, we use $g_{\perp} = 3.06$ and $g_{||} = 3.72$ (*25*). As we discuss below, the disorder present in $YbMgGaO_4$ introduces a significant variation in the value of these Hamiltonian parameters. We introduce quenched disorder in the exchange interactions (J-disorder) and in the g-factors (g-disorder). We assume that both have a uniform distribution of predefined width around the aforementioned mean values, $(g_{\perp})_i = (g_{\perp})_{av} + \Delta_i(\sigma_{g_{\perp}})$, $(g_{||})_i = (g_{||})_{av} + \Delta_i\left(\sigma_{g_{||}}\right)$, and $J_{ij} = J_{av}\left(1 + \Delta_{ij}(\sigma_J)\right)$, where $\sigma_{g_{\perp}} = 0.3$, $\sigma_{g_{||}} = 1.2$ and $\sigma_J = 0.5$.

The static magnetic structure factor $S(\boldsymbol{Q})$ is calculated by a standard Metropolis sampling algorithm while the dynamical structure factor $S(\boldsymbol{Q}, \omega)$ is computed by Landau-Lifshitz dynamics (*27*). Both types of structure factors shown throughout this paper are calculated by averaging over 60 independent sets of 2000 configuration samples from a standard Metropolis sampling algorithm on a 48×48 supercell (2304 spins), followed by a slow annealing process starting from a random disordered spin configuration.

To account for the effects of quantum fluctuations, we have computed the $M(H)$ curve with the DMRG method on the $S = 1/2$ version of H (without disorder), for field directions parallel to the c-axis and to the ab-plane. The resulting $M(H)$ curve exhibits a characteristic plateau at 1/3 of the saturation value (*27*, *28*), which is bigger for $H \perp c$ because of the easy-plane anisotropy (Fig. 3). This plateau phase is a true quantum mechanical signature: quantum fluctuations favor collinear configurations. The effect of quantum fluctuations can then be reproduced by adding an effective bi-quadratic interaction to the classical Hamiltonian (*29*, *30*),

$$H_1 = H - \lambda_1 \sum_{\{ij\}} \left(S_i.S_j\right)^2 - \lambda_2 \sum_{\{ij\}_2} \left(S_i.S_j\right)^2,$$

where H is the classical spin Hamiltonian given in Eq. (1) and $\lambda_1 = 0.3J_\pm$ and $\lambda_2 = 0.03\,J_\pm$ are effective bi-quadratic couplings for next and second nearest-neighbor spins, respectively. The values of λ_1 and λ_2 have been obtained by comparing the $M(H)$ curve obtained with DMRG for the $S = 1/2$ version of H and the $M(H)$ curve obtained from a classical MC simulation of H_1.

To compare the calculations and TDO magnetic susceptibility results, we subtract T = 4 K measurement as background from the T = 0.35 K data, then integrating with respect to applied field yield a curve proportional to magnetization (Fig. 4). The extracted magnetization curve shows a distinct non-linearity that can be seen in the low-temperature calculation result, which is performed in the absence of site disorder. These results suggest that the absence of the feature in $M(H)$ curves noted in earlier work (*15, 17, 21*), is due to thermal fluctuations (since these were measured from 1.7 K to 2 K), though we note the 0.5 K curve in (*20*) corroborates our results. It seems lower temperature and more sensitive techniques are required to observe the anomaly clearly. Crucially, comparison of calculated $S(\boldsymbol{Q})$ in the absence of disorder at T = 0 (Fig. S8) to T = 130 mK (Fig. S9) shows that small temperatures are enough to disrupt long-range order, owing to the high degree of frustration. These effects are likely enhanced by quenched disorder, which is essential to reproduce the broadening of the magnon peaks (Fig. S7) at H = 7.8 T as also observed in experiment (*15*).

In summary, our work suggests that the spin liquid signatures observed in $YbMgGaO_4$ can arise from high frustration working in concert with thermal fluctuations even at very low temperatures, and that these effects are likely enhanced by the inherent quenched disorder of the system. Field induced phase transitions were proven as an effective probe in unveiling the true nature of the ground state in $YbMgGaO_4$.

References and Notes:

1. Y. Zhou, K. Kanoda, T.-K. Ng, "Quantum spin liquid states." *Rev. Mod. Phys.* **89**, 025003 (2017).
2. L. Savary, L. Balents, Quantum spin liquids: a review. *Rep. Prog. Phys.* **80**, 016502 (2016).
3. J. Iaconis, C. Liu, G. Halász, L. Balents, Spin liquid versus spin orbit coupling on the triangular lattice. *SciPost Phys.* **4**, 003 (2018).
4. R. Kaneko, S. Morita, M. Imada, Gapless spin-liquid phase in an extended spin 1/2 triangular Heisenberg model. *J. Phys. Soc. Japan* **83**, 093707 (2014).
5. Z. Zhu, P. Maksimov, S. R. White, A. L. Chernyshev, Disorder-induced mimicry of a spin liquid in $YbMgGaO_4$. *Phys. Rev. Lett.* **119**, (2017).
6. Z. Zhu, P. A. Maksimov, S.n R. White, A. L. Chernyshev. Topography of spin liquids on a triangular lattice. *Phys. Rev. Lett.* **120**, 207203 (2018).
7. Y.-D. Li, Y.-M. Lu, G. Chen, Spinon Fermi surface U(1) spin liquid in the spin-orbit-coupled triangular-lattice Mott insulator YbMgGaO4. *Phys. Rev. B* **96**, 054445 (2017).
8. I. Kimchi, A. Nahum, T. Senthil, Valence bonds in random quantum magnets: theory and application to $YbMgGaO_4$. *Phys. Rev. X* **8**, 031028 (2018).
9. E. Parker, L. Balents, Finite-temperature behavior of a classical spin-orbit-coupled model for $YbMgGaO_4$ with and without bond disorder. *Phys. Rev. B* **97**, 184413 (2018).

10. Q. Luo , S. Hu, B. Xi, J. Zhao, X. Wang, Ground-state phase diagram of an anisotropic spin-1/2 model on the triangular lattice. *Phys. Rev. B* **95**, 165110 (2017).

11. Y.-D. Li, Y. Shen, Y. Li, J. Zhao, G. Chen, Effect of spin-orbit coupling on the effective-spin correlation in $YbMgGaO_4$. *Phys.Rev. B* **97**, 125105 (2018).

12. Z.-X. Luo, E. Lake, J.-W. Mei, O. A. Starykh, Spinon Magnetic Resonance of Quantum Spin Liquids. *Phys. Rev. Lett.* **120**, 037204 (2018).

13. Y. Shen, Y.-D. Li, H. C. Walker, P. Steffens, M. Boehm, X. Zhang, S. Shen, H. Wo, G. Chen, J. Zhao, Fractionalized excitations in the partially magnetized spin liquid candidate $YbMgGaO_4$. Nat. Comm. **9**, 1 (2018) 4138.

14. Y. Li, D. Adroja, P. K. Biswas, P. J. Baker, Q. Zhang, J. Liu, A. A. Tsirlin, P. Gegenwart, Q. Zhang, Muon spin relaxation evidence for the U(1) quantum spin-liquid ground state in the triangular antiferromagnet YbMgGaO4. *Phys. Rev. Lett.* **117**, 097201 (2016).

15. J. A. M. Paddison, M. Daum, Z. Dun, G. Ehlers, Y. Liu, M. B. Stone, H. Zhou, M. Mourigal, Continuous excitations of the triangular-lattice quantum spin liquid YbMgGaO4. *Nat. Phys.* **13**, 117-122 (2017).

16. Y. Li, D. Adroja, R. I. Bewley, D. Voneshen, A. A. Tsirlin, P. Gegenwart, Q. Zhang, Crystalline electric-field randomness in the triangular lattice spin-liquid $YbMgGaO_4$. *Phys. Rev. Lett.* **118**, 107202 (2017).

17. Y. Shen., Y.-D. Li, H. Wo, Y. Li, S. Shen, B. Pan, Q. Wang, H. C. Walker, P. Steffens, M. Boehm, Y. Hao, D. L. Quintero-Castro, L. W. Harriger, M. D. Frontzek, L. Hao, S. Meng, Q. Zhang, G. Chen, J. Zhao, Evidence for a spinon Fermi surface in a triangular-lattice quantum-spin-liquid candidate. *Nature* **540**, 559-562 (2016).

18. Y. Li, D. Adroja, D. Voneshen, R. I. Bewley, Q. Zhang, A. A. Tsirlin, P. Gegenwart, Nearest-neighbour resonating valence bonds in YbMgGaO4. *Nat.Comm.* **8**, 15814 (2017).

19. Y. Xu, J. Zhang, Y.S. Li, Y. J. Yu, X. C. Hong, Q. M. Zhang, S. Y. Li, Absence of magnetic thermal conductivity in the quantum spin-liquid candidate $YbMgGaO_4$. *Phys. Rev. Lett.* **117**, 267202 (2016).

20. Y. Li, H. Liao, Z. Zhang, S. Li, F. Jin, L. Lin, L. Zhang, Y. Zou, L. Pi, Z. Yang, J. Wang, Z. Wu, Q. Zhang, Gapless quantum spin liquid ground state in the two-dimensional spin-1/2 triangular antiferromagnet YbMgGaO4. *Sci. Rep.* **5**, 16419 (2015).

21. Y. Li, G. Chen, W. Tong, L. Pi, J. Liu, Z. Yang, X. Wang, Q. Zhang, Rare-earth triangular lattice spin liquid: a single-crystal study of $YbMgGaO_4$. *Phys. Rev. Lett.* **115**, 167203 (2015).

22. Y-D. Li, X. Wang, G. Chen. Anisotropic spin model of strong spin-orbit-coupled triangular antiferromagnets. Phys. Rev. B 94, 035107 (2016).

23. X. Zhang, F. Mahmood, M. Daum, Z. Dun, J. A. M. Paddison, N. J. Laurita, T. Hong, H. Zhou, N. P. Armitage, M. Mourigal, Hierarchy of exchange interactions in the triangular-lattice spin liquid $YbMgGaO_4$. *Phys. Rev. X* **8**, 031001 (2018).

24. H. Srikanth, J. Wiggins, H. Rees, Radio-frequency impedance measurements using a tunnel-diode oscillator technique. *Rev. Sci. Instrum* **70**, 3097-3101 (1999).

25. S. Tóth, K. Rolfs, A. R. Wildes, C. Rüegg, Strong exchange anisotropy in YbMgGaO4 from polarized neutron diffraction. *arXiv:1705.05699*, (2017).

26. A. M. Samarakoo, A. Banerjee, S.-S. Zhang, Y. Kamiya, S.E. Nagler, D. A. Tennant, S.-H. Lee, C. D. Batista, Comprehensive study of the dynamics of a classical Kitaev spin liquid. *Phys.Rev. B* **96**, 134408 (2017).

27. A. V. Chubukov, D. I. Golosov, Quantum theory of an antiferromagnet on a triangular lattice in a magnetic field. *J. Phys.-Condens. Mat.* **3**, 69–82 (1991).

28. Y. Kamiya, L. Ge, T. Hong, Y. Qiu, D. L. Quintero-Castro, Z. Lu, H. B. Cao, M. Matsuda, E. S. Choi, C. D. Batista, M. Mourigal, H. D. Zhou, J. Ma, The nature of spin excitations in the one-third magnetization plateau phase of $Ba_3CoSb_2O_9$. *Nat. Commun.* **9**, 2666 (2018).

29. C. Griset, S. Head, J. Alicea, O. A. Starykh, Deformed triangular lattice antiferromagnets in a magnetic field: Role of spatial anisotropy and Dzyaloshinskii-Moriya interactions. *Phys. Rev. B* **84**(24), 245108. (2011).

30. T. Nikuni, A. E. Jacobs, Quantum fluctuations in the incommensurate phase of $CsCuC_{l3}$ in a transverse magnetic field. *Phys.Rev. B* **57**, 5205-5212 (1998).

31. J. Rodriguez-Carvajal, Recent Advances in magnetic structure determination by neutorn powder diffraction. *Physica B.* **192.** 55-69 (1993)

32. C. T. Van Degrift, Tunnel diode oscillator for 0.001 ppm measurements at low temperatures. *Rev. Sci. Instrum.* **46** 599-607 (1975).

33. E. Ohmichi, T. Osada, Torque magnetometry in pulsed magnetic fields with use of a commercial microcantilever. *Rev. Sci. Instrum.* **73**, 3022-3026 (2002).

34. S. Rosenkranz, R. Osborn, Correlli: Efficient single crystal diffraction with elastic discrimination. *Pramana* **71**, 705-711 (2008).

35. T. M. Michels-Clark, A.T. Savici, V.E. Lunch, X. Wang, C. M. Hoffmann, Expanding Lorentz and spectrum corrections to large volumes of reciprocal space for single-crystal time-of-flight neutron diffraction. *J. Appl. Crystallogr.* **49**, 497-506 (2016)

Acknowledgements:

We are grateful to Andrei T. Savici for help in analyzing the neutron scattering data. A portion of this work was performed at the National High Magnetic Field Laboratory, which is supported by the National Science Foundation Cooperative Agreement No. DMR1157490 and DMR-1644779, the State of Florida and the U.S. Department of Energy. A portion of this research used resources at the Spallation Neutron Source, a DOE Office of Science User Facility operated by the Oak Ridge National Laboratory. W.M.S., Z.S., C.M., and S.H. acknowledge support provided by funding from the Powe Junior Faculty Enhancement Award, and William M. Fairbank Chair in Physics at Duke University. A.S. and C.D.B. were partially funded by the U.S. Department of Energy Office of Basic Energy Sciences. C.D.B. also acknowledges support from the LANL Directed Research and Development program.

Author contributions: S.H. conceived and supervised the project. W.M.S., S.D., Y.L., and S.H. performed neutron scattering experiments and analyzed the results. Z.S., D.G., W.M.S., and S.H. performed magneto-transport measurements and analyzed the results. C.M. and S.H. grow the single crystal sample. A.S. and C.D.B. performed MC calculations and provided theoretical interpretation. W.Z. performed DMRG calculations. W.M.S. and A.S. made the figures. W.M.S., C.D.B. and S.H. wrote the paper with input from all authors.

Competing interests: Authors declare no competing interests.

Data and materials availability: The data that support the findings of this study are available from the corresponding author upon request.

Supplementary Materials:

Materials and Methods

Fig. S1 – S9

Reference (31 – 35)

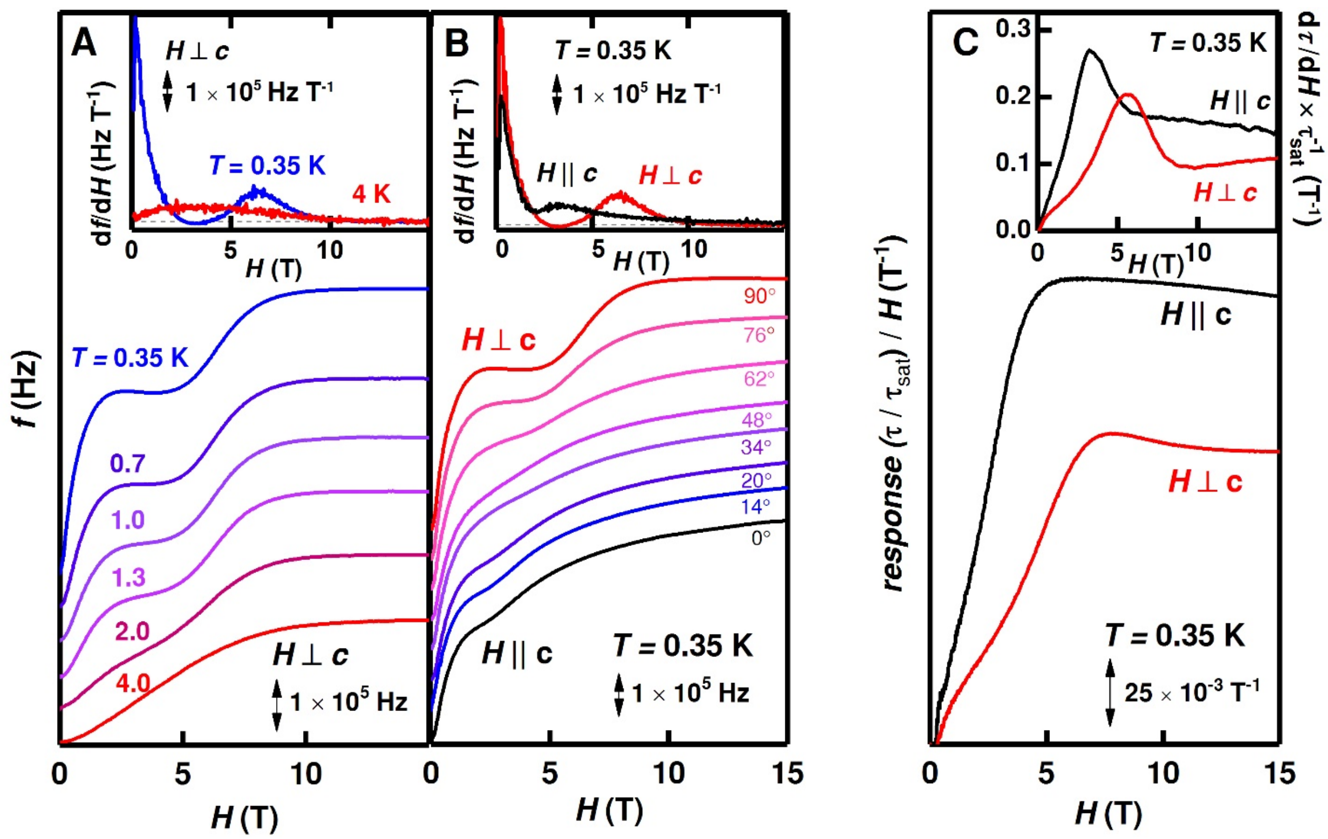

Fig. 1. TDO frequency and cantilever torque response versus applied field. (**A**) TDO ($\Delta f/f \propto \Delta M/\Delta H$) shows an anomaly for $H \perp c$ axis which weakens as temperature increases (curves offset for clarity in (**A**), (**B**)). (**B**) Anomaly's response to applied field shows anisotropy. (**C**) Normalized cantilever response divided by H (See Materials and Methods in Supplementary Materials), confirms the anomaly measured with TDO.

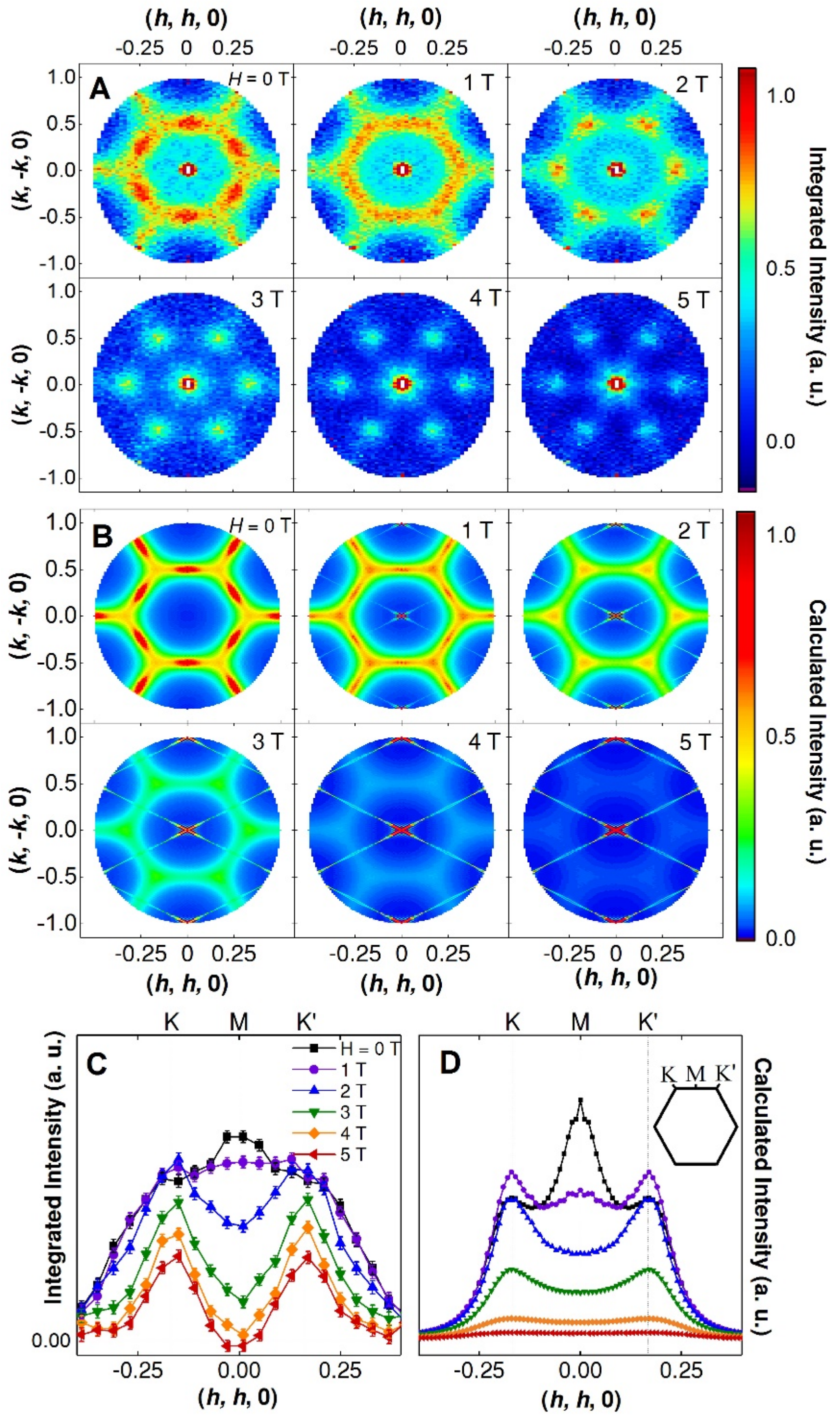

Fig. 2. Diffuse neutron scattering from magnetic structure for a series of fields with $H||c$. (**A**) Color maps of Brillouin zone integrated (-0.5 < l < 0.5). As field increases, spectral weight shifts from M points to K points, then Γ points, in agreement with (**B**) calculated $S(\boldsymbol{Q})$ with $\sigma_{g_\perp} =$

0.3, $\sigma_{g_{||}} = 1.2$, and $\sigma_J = 0.5$ at 130 mK. (**C**) Integrated neutron scattering intensity (-0.5 < l < 0.5) along $(h, h, 0)$ direction. (**D**) Calculated $S(\boldsymbol{Q})$ along $(h, h, 0)$.

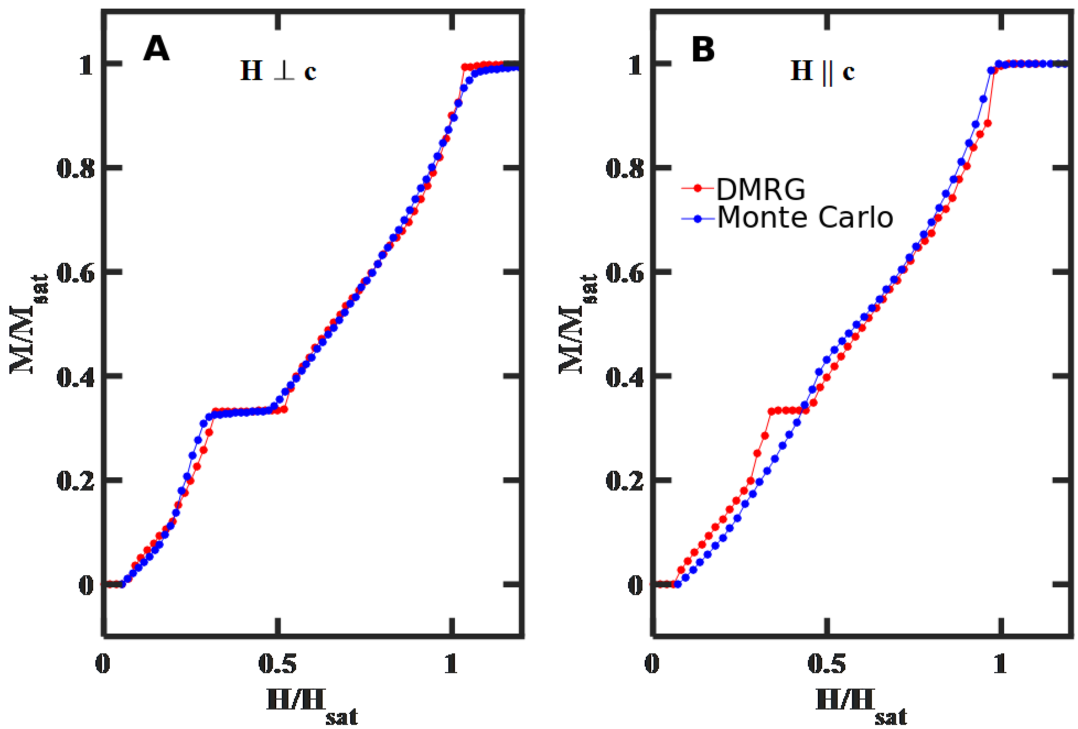

Fig. 3. Magnetization curves obtained with Monte Carlo sampling and DMRG. Comparison of magnetization from DMRG calculations (red) versus classical simulations with bi-quadratic interaction ($\lambda_1 = 0.3,\ \lambda_2 = 0.03$) when (**A**) $H \perp c$ and (**B**) $H \mid\mid c$. Addition of bi-quadratic terms mimics quantum mechanical plateau for applied field perpendicular to sample c axis.

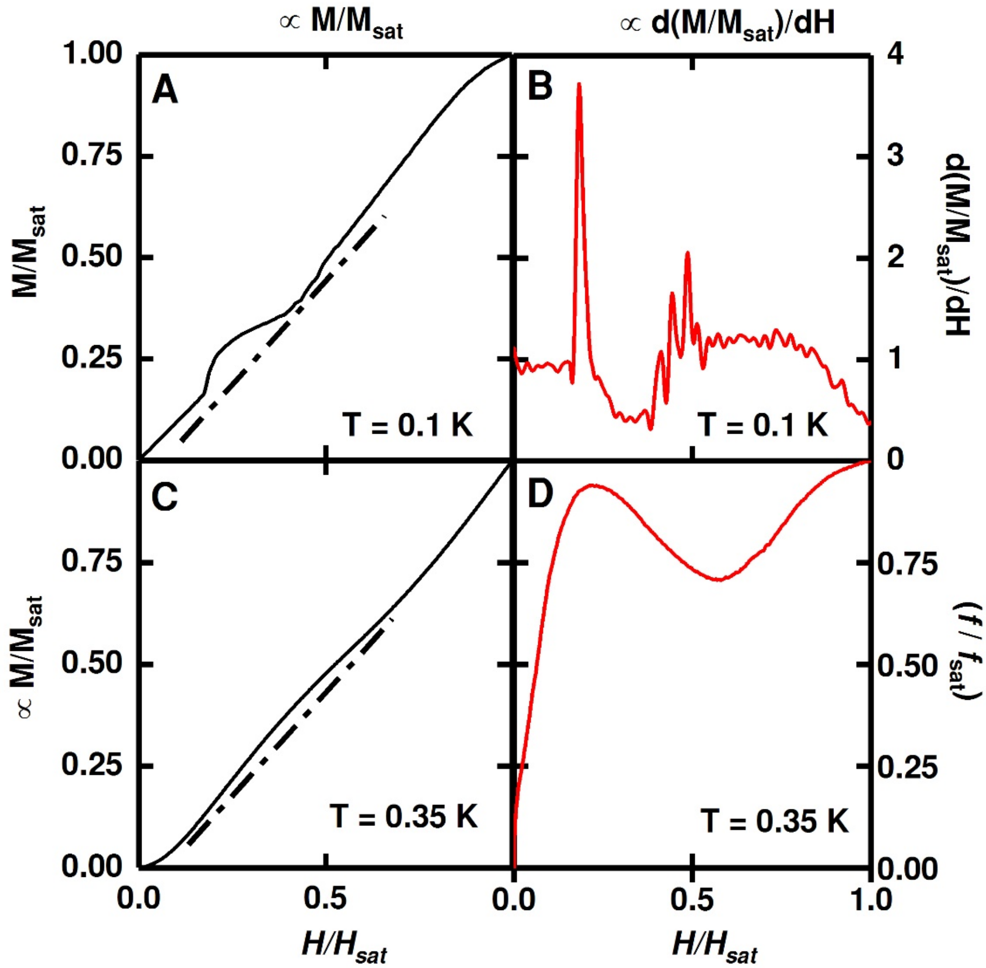

Fig. 4. Calculated magnetization curves and background-subtracted integrated TDO measurement for $H \perp c$. (**A**) Classical Monte Carlo simulation of magnetization (featuring bi-quadratic terms but no disorder) at $T = 0.1$ K. Dashed line highlights non-linearity. (**B**) Derivative with respect to applied field of classical Monte Carlo simulation in (**A**). (**C**) Integration of 4 K background-subtracted TDO frequency at $T = 0.35$ K. Non-linearity broadened and suppressed by disorder. **(D)** TDO response frequency at $T = 0.35$ K with 4 K data subtracted as background.

Supplementary Materials for

Field-Induced Phase Transition of the Spin Liquid State in Triangular Antiferromagnet $YbMgGaO_4$

Authors: William M. Steinhardt[1], Zhenzhong Shi[1], Anjana Samarakoon[2,3], Sachith Dissanayake[1,3], David Graf[4], Yaohua Liu[3], Wei Zhu[5,6], Casey Marjerrison[1], Cristian D. Batista[2,7], Sara Haravifard[1,8*]

Affiliations:

[1] Department of Physics, Duke University, Durham, North Carolina 27708, USA.

[2] Shull-Wollan Center, Oak Ridge National Laboratory, Oak Ridge, Tennessee 37831, USA.

[3] Neutron Scattering Division, Oak Ridge National Laboratory, Oak Ridge, Tennessee 37831, USA.

[4] National High Magnetic Field Laboratory and Department of Physics, Florida State University, Tallahassee, Florida 32310, USA.

[5] Theoretical Division, T-4 & CNLS, Los Alamos National Laboratory, Los Alamos, New Mexico 87545, USA.

[6] Westlake Institute of Advanced Study, Hangzhou 310024, China.

[7] Department of Physics, University of Tennessee, Knoxville, Tennessee 37996, USA.

[8] Department of Mechanical Engineering and Materials Science, Duke University, Durham, North Carolina 27708, USA.

* Correspondence to: haravifard@phy.duke.edu

This PDF file includes:

Materials and Methods
Figs. S1 to S9

Materials and Methods

Sample Synthesis and Preliminary Characterization

Powder of $YbMgGaO_4$ (structure shown in Fig. S1) was produced by finely grinding mixed powders of Yb_2O_3, MgO, and Ga_2O_3, and reacting at 1150° C in a box furnace. The product was ground again to a fine powder, compressed hydrostatically into a rod, and then sintered at 1500° C in a vertical Bridgman furnace. Finally, large single-crystals of $YbMgGaO_4$ were grown using the optical floating zone method (Fig. S2). A typical crystal was grown in an O_2 atmosphere at 1 MPa, with an initial growth speed of 20 mm/hr, and upon stabilization of the liquid zone, ~ 4 mm/hr until finished.

We confirmed the powder and crystal phase at each step of the synthesis using ground powders and the Panalytical X'Pert PRO X-ray diffraction system (using Cu K-α 1.5418 nm X-rays) and Rietveld refinement via FULLPROF (*31*). Single-crystal quality and alignment was determined using Laue X-ray diffraction (Fig. S3B). Preliminary susceptibility measurements were carried out on a powder sample using a Quantum Design MPMS SQUID magnetometer down to 1.8 K, and confirmed previous measurements of the Curie-Weiss temperature $\Theta \approx -4$ K.

High-Sensitivity Magneto-Transport Measurements

High-sensitivity measurements of magnetic susceptibility were achieved with the complimentary tunnel diode oscillator (TDO) technique and torque magnetometry. In a TDO measurement, a tunnel diode is biased to operate in the "negative resistance" region of the IV-curve. This provides power that maintains the resonance of a *LC*-circuit at a frequency range between 10 and 50 MHz. An approximately cylindrical single crystal sample with dimensions of ~2 mm in length and ~1 mm in diameter was placed inside a detection coil, with the *c* axis of the sample aligned with the coil axis (Fig. S5A). Together, they form the inductive component of the *LC*-circuit. Changes in sample magnetization induce a change in the inductance, hence a shift in the resonance frequency. Highly sensitive measurements in changes of magnetic moments ~ 10^{-12} e.m.u., therefore, are enabled by the ability of measuring the resonance frequency to a high precision (*32*).

Torque magnetometry (Fig. S5B) is another valuable tool to probe magnetically anisotropic materials. Here, commercial piezoresistive cantilevers (produced by Seiko and SCL-Sensor Tech) (*33*) were used, where a piezoresistive element at the base of the cantilever senses the deflection of the arm, induced by the magnetic torque of the 30 x 70 x 70 μm^3 crystal at the other end of the 300-400 μm long cantilever arm. A second piezoresistive element on the same cantilever assembly, not attached to any sample, provides a zero-torque reference. These two piezoresistive elements along with two potentiometers at room temperature are used to build a Wheatstone bridge, which is balanced to provide a null signal at zero magnetic field. At finite field, the sample experiences a magnetic torque, which results in a finite voltage across the bridge. The susceptibility anisotropy is in proportion to the measured voltage response of the bridge divided by the applied magnetic field.

Using cantilever torque magnetometry to measure directly the sample magnetization is extremely challenging due to the requirements of extremely small sample size and precise calibration of the cantilever. However, the measurement provides a straight-forward way of corrobating features observed in TDO mesurements. In Fig. 1C of the main text, we plot the normalized cantilever response divided by H, where the responses are normalized according to their saturation field, determined by the condition that the second derivative of the response is close to zero (less than 1.25 μV, where the curve is essentially flat). This accounts for the differing response of the cantilever arm as it is rotated with respect to field (both measurements are of the same sample, so mass may be neglected). Dividing by H yields a quantity directly proportional to the anisotropy of magnetic response as seen from $\tau = M \times H$.

<u>Neutron Scattering</u>

Neutron scattering data was collected at the CORELLI spectrometer at Spallation Neutron Source, Oak Ridge National Laboratory (*34*). CORELLI is a quasi-Laue time-of-flight instrument equipped with a large 2D detector, with a -20° to +150° in-plane coverage and $+/-28.5°$ out-of-plane coverage. The incident neutron energy was between 10 meV and 200 meV. A superconducting magnet was used to provide a vertical magnetic field up to 5 T, which reduced the effective out-of-plane coverage to $\pm$ 8°. An 896.10 mg single crystal was mounted on a Cu plate in a dilution refrigerator. The sample was aligned with the (*h*, *h*, *l*) plane horizontal and the magnetic field along the [1 -1 0] direction. Neutron-absorbing Cd was used to shield the sample holder to reduce the background scattering. Experiments were conducted with applied fields at the base temperature 130 mK by rotating the crystal through 180° in 3° steps, and then at 20 K in the same fields for background subtraction. The data were reduced using Mantid for the Lorentz and spectrum corrections (*35*).

To account for the temperature factor in our background subtraction in total-scattering mode, we compared the ratio of integrated intensities of a small background region in reciprocal space at 5 T for both temperatures. The region was bounded by $-0.9 < h < -0.75$, $0.75 < k < 1.1$, and $-0.5 < l < 0.5$; the l range is consistent with our Brillouin Zone (BZ) edge and planar integrations. We used the second BZ and 5 T data to avoid skewing the integration at low temperature due to diffuse magnetic scattering. This integration approximates the ratio of Bose population factors - our scaling factor was 1.133 ± 0.005. To improve statistics, we used the 6-fold symmetry (in accordance to the crystallographic symmetry of the sample) to add our data 6 times at subsequent 60° angles and average. All analysis and visualization were performed using Mantid and Python. The background subtracted data before symmetry operations is shown in Fig. S6, and after symmetry operations (with higher statistics) is shown in Fig. 2 of the main text.

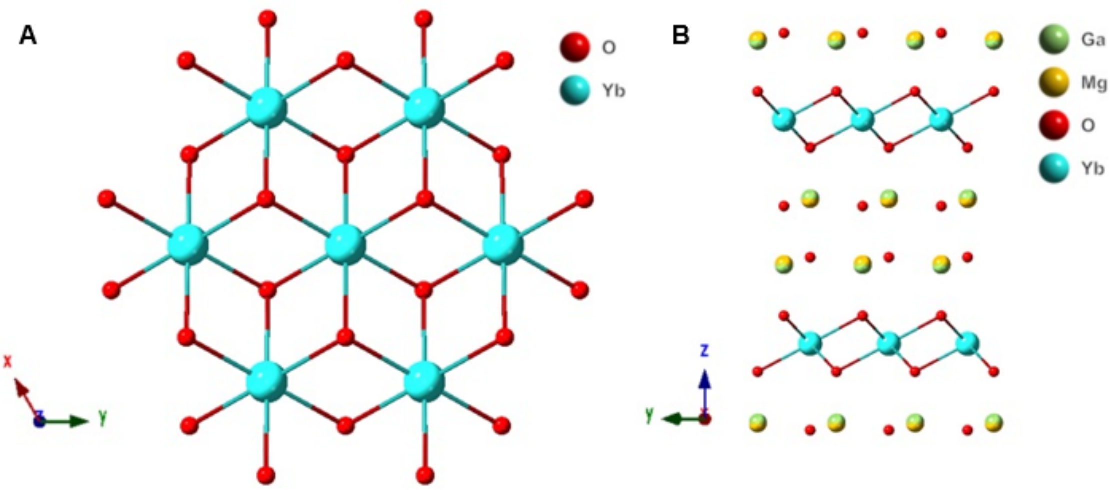

Fig. S1. Structure of $YbMgGaO_4$. (**A**) View of *ab* plane of magnetic Yb^{3+} ions (teal) with coordination by oxygen (red) on a triangular lattice. (**B**) View of $YbMgGaO_4$ structure perpendicular to *c* axis. Mixed yellow and green spheres indicate sites of split occupancy of Mg^{2+} and Ga^{3+}, separating the planes of magnetic Yb^{3+} ions.

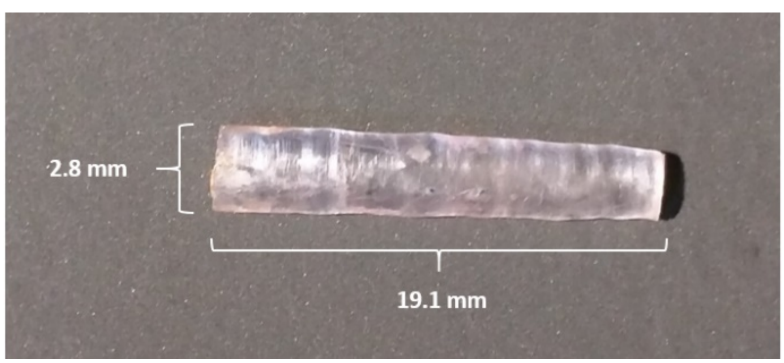

Fig. S2. Single crystal sample. A large single crystal of $YbMgGaO_4$ grown using the floating zone method – sample mass is approximately 0.9 g.

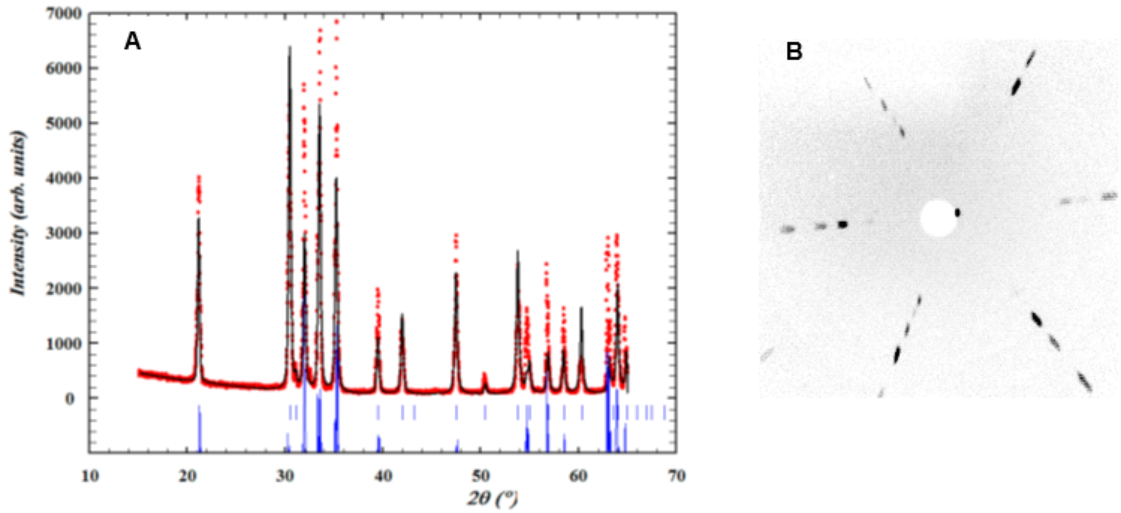

Fig. S3. Xray Diffraction Results. (**A**) Rietfeld analysis of powder X-ray diffraction data confirms the pure phase of the sample. (**B**) Laue X-ray image confirms the high quality of the single crystal, showing hexagonal symmetry of the ab plane (central peak is [001]).

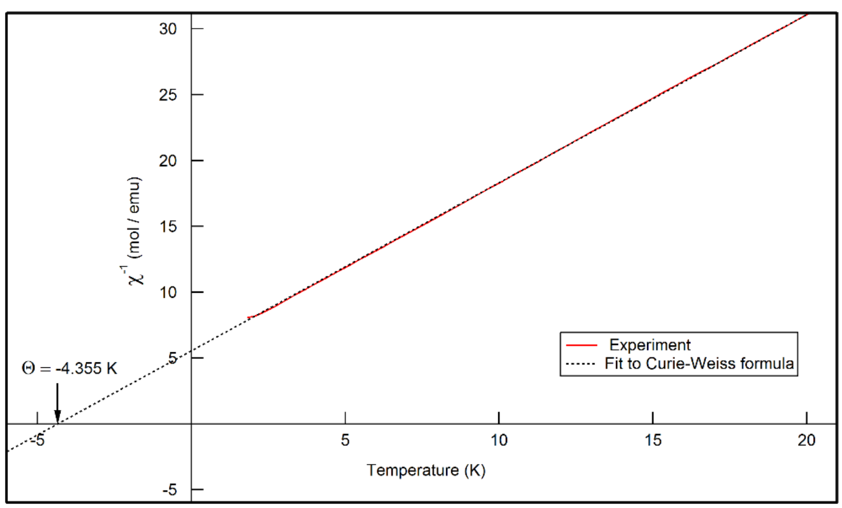

Fig. S4. Low temperature fit of inverse susceptibility for powder sample. Measured Curie-Weiss temperature of $\Theta \approx -4\ K$ demonstrates antiferromagnetic interactions.

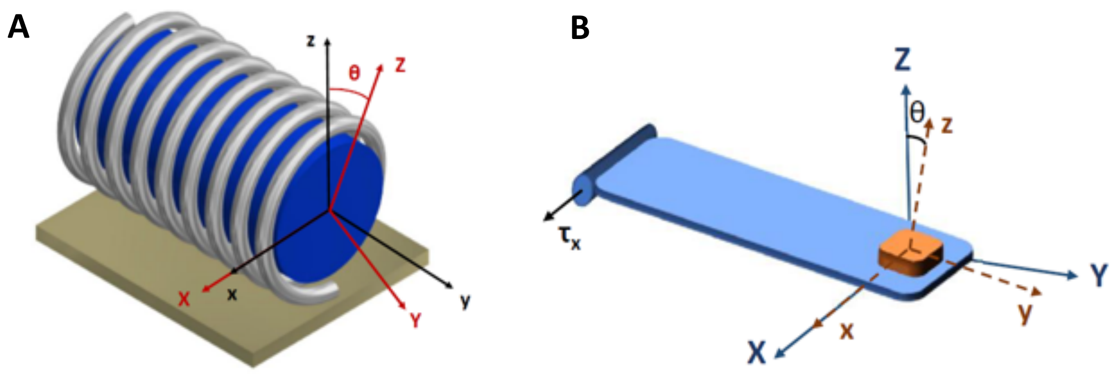

Fig. S5. Magnetic susceptibility measurement techniques. (**A**) Schematic of tunnel diode oscillator coil with sample inserted. Red, dashed lines indicate lab frame, while black coordinate axes refer to the sample frame. Supposing the applied field is along *z* in the lab frame, θ is the angle the field makes with a reference lattice direction. (**B**) Schematic of cantilever torque magnetometry – coordinate systems are as described in (**A**).

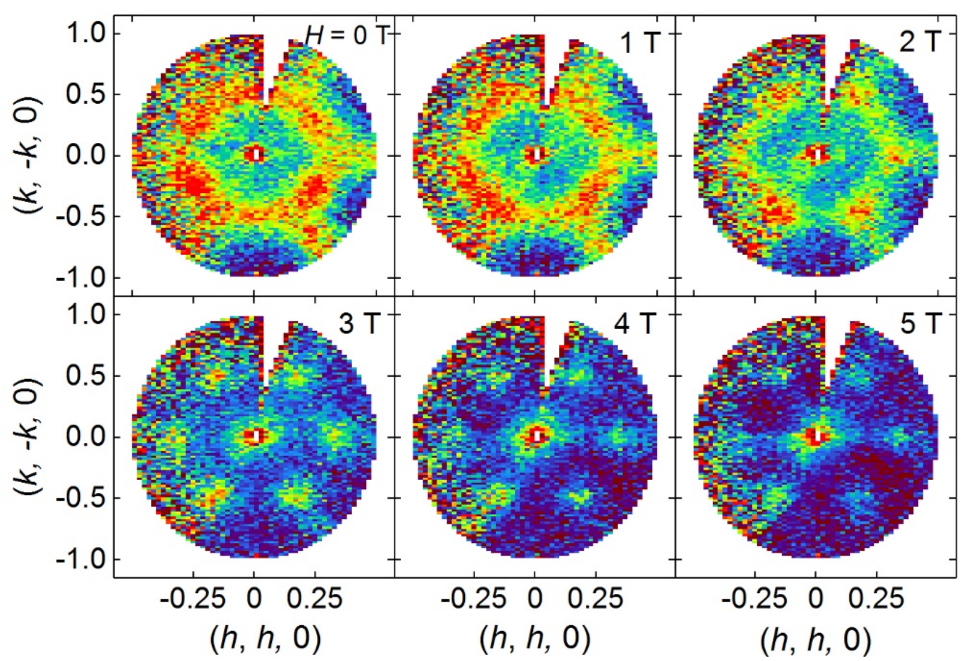

Fig. S6. Diffuse neutron scattering for a series of fields. Intensity integrated ($-0.5 < l < 0.5$), background subtracted and normalized data shows the first BZ for integer fields from 0 to 5 T. The data was collected by rotating the crystal through 180° in 3° steps at 130 mK. Corresponding 20 K date was collected and subtracted as background, to isolate the magnetic response. The 6-fold rotation symmetry operations were applied to the data shown here in order to increase statistics as shown in Fig. 2 of the main text.

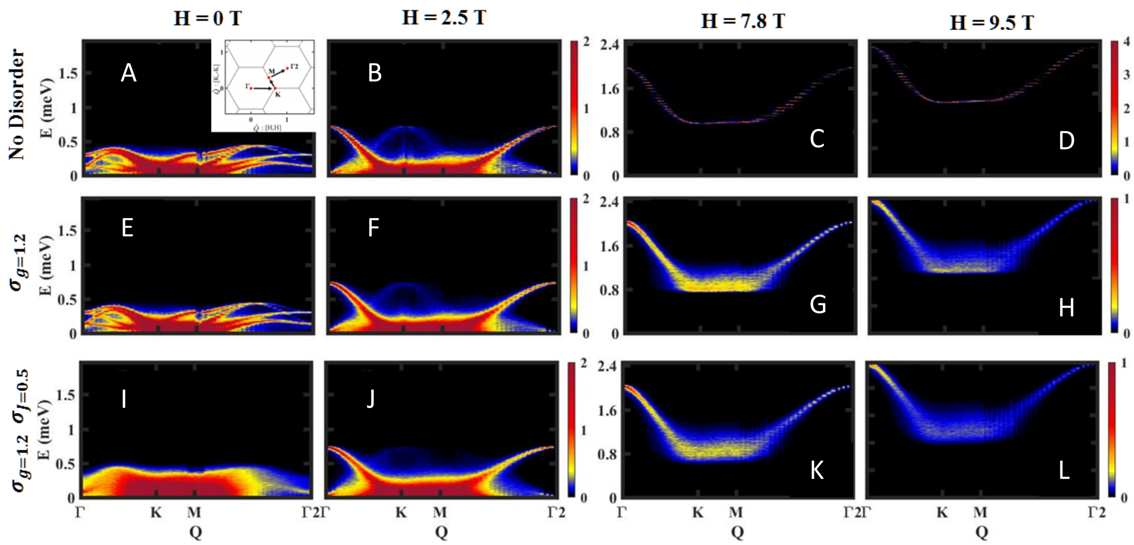

Fig. S7. $S(\boldsymbol{Q},\boldsymbol{\omega})$ along a high-symmetry path in reciprocal space. $S(\boldsymbol{Q},\omega)$ as a function of magnetic field, and different disorder conditions; for disorder free model at (**A**) $H = 0$, (**B**) 2.5 T, (**C**) 7.8 T and (**D**) 9.5 T; for the model with g-disorder of σ_g =1.2 at (**E**) $H = 0$, (**F**) 2.5 T, (**G**) 7.8 T and (**H**) 9.5 T; and for the model with g-disorder of $\sigma_g = 1.2$ at (**I**) H = 0, (**J**) 2.5 T, (**K**) 7.8 T and (**L**) 9.5 T. The high-symmetry path is shown in the insert of panel (**A**).

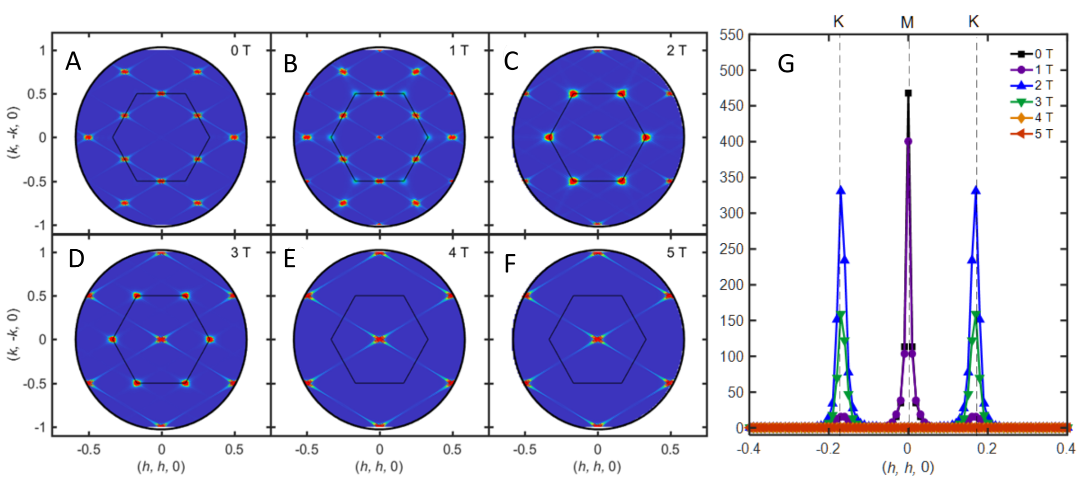

Fig. S8. Magnetic field dependence of $S(\boldsymbol{Q})$ for the disorder free model at $\boldsymbol{T} = 0$. (**A**) $H = 0$, (**B**) 1 T (**C**) 2 T (**D**) 3 T, (**E**) 4 T and (**F**) 5 T. (**G**) shows $S(\boldsymbol{Q})$ integrated along l direction and plotted along (h, h, 0) direction for different magnetic field values.

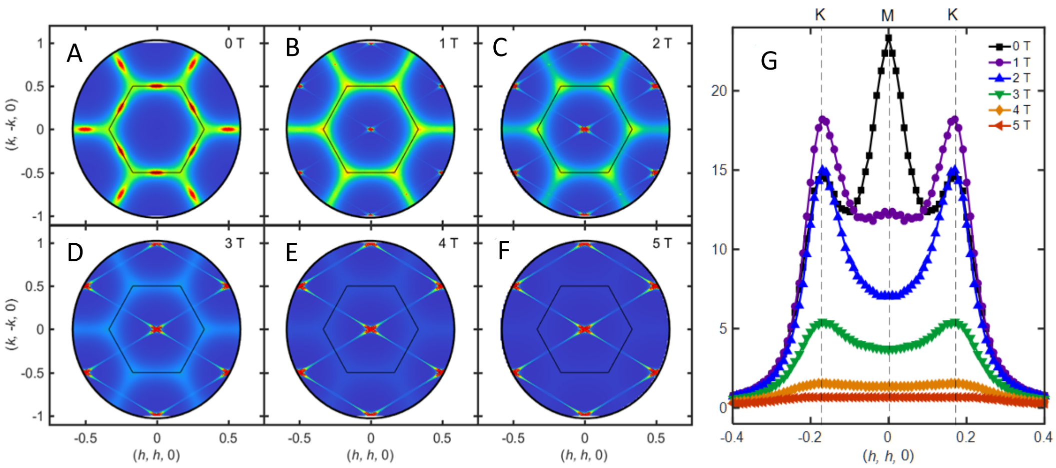

Fig. S9. Magnetic field dependence of $\boldsymbol{S(Q)}$ for the disorder free model at $\boldsymbol{T}$ = 0.130 K. (**A**) $H = 0$, (**B**) 1 T (**C**) 2 T (**D**) 3 T, (**E**) 4 T and (**F**) 5 T. (**G**) shows $S(\boldsymbol{Q})$ integrated along l direction and plotted along (h, h, 0) direction for different magnetic field values.